Aerospace Science and Technology 172 (2026) 111699

Contents lists available at ScienceDirect

Aerospace Science and Technology

journal homepage: www.elsevier.com/locate/aescte

Original article

Directional noise reduction via rotor phase–shifting for multirotor aircraft

Francesco Sessini [a], Diego Donnini [a], Aldo Chella [a], Thorsten Schwarz [b], Jianping Yin [b], Gabriele Bellani [a], Emanuele L. de Angelis [a,*]

[a] University of Bologna, Department of Industrial Engineering (DIN), CIRI Aerospace, Forlí, 47121, Italy
[b] German Aerospace Center (DLR), Institute of Aerodynamics and Flow Technology, Helicopter Department, Braunschweig, 38108, Germany

ARTICLE INFO

Editor: Dr. Duc Dinh Nguyen

Keywords:
Urban air mobility
Aeroacoustics
Rotor phase synchronization
Active noise reduction
VTOL

ABSTRACT

This study investigates rotor phase synchronization as a strategy for directional noise reduction in multirotor vertical take–off and landing (VTOL) aircraft employing collective pitch control. The application of this approach enables the redirection of acoustic emissions away from noise–sensitive regions without degrading aerodynamic performance or requiring alterations to the flight trajectory. A dedicated simulation framework integrates the mid–fidelity aerodynamic solver UPM with the aeroacoustic prediction model APSIM, developed at the German Aerospace Center (DLR), Institute of Aerodynamics and Flow Technology. To reproduce representative flight conditions, a trimming procedure determines the required control inputs and vehicle attitude. Such simulation methodology was validated by reproducing available experimental data for hovering fixed–pitch propellers. To identify optimal rotor phasing for noise redirection in full–scale quadrotor and hexarotor configurations under trimmed flight conditions, two distinct optimization strategies are employed. In forward flight, optimization is conducted using the complete high–fidelity simulation environment. For hover conditions, an analytical aeroacoustic model based on compact source theory provides a computationally efficient alternative that reduces the demands placed on the optimizer. Acoustic pressure evaluations on a ground plane beneath the vehicle confirm that optimized rotor phasing successfully redirects noise away from designated regions.

1. Introduction

Urban Air Mobility (UAM) represents one of the most promising and rapidly evolving areas of research in the aerospace industry. Advanced vertical take–off and landing (VTOL) vehicles are expected to become integral components of future transportation systems, offering solutions to urban congestion and increasing accessibility to remote areas. However, a great challenge in the deployment of these vehicles is mitigating noise emissions, as they will operate in close proximity to populated areas where public acceptance is a key determinant of their success. Studies, including NASA market research [1], have identified noise as a critical obstacle to the commercialization of UAM aircraft. Public concerns about the disruptive effects of aircraft noise in densely populated environments together with regulatory approval underscore the need for quieter designs [2].

The primary objective of this research is to develop a numerical simulation framework capable of assessing noise–canceling strategies across various multirotor configurations. Specifically, the study focuses on investigating the effect of rotor phase–shifting on noise directivity for multirotor configurations.

The issue of noise generation by VTOL vehicles has been extensively addressed in the literature, with various mitigation strategies proposed over the years [3–5]. Most of these approaches are passive, for example in [6], an optimization of the rotor blade planform is carried out to minimize the acoustic emission while retaining aerodynamic performance. More recently, however, an active noise reduction technique known as rotor phase synchronization has gained significant attention, particularly in the context of electric multirotor vehicles for Urban Air Mobility [7–15].

This method exploits the rotors as coherent sound sources to create destructive interference of sound waves at selected observer positions, as schematically depicted in Fig. 1. The aim is to steer tonal noise away from designated areas around the vehicle by adjusting the phase angle of rotors operating at the same rotational speed. Experimental and numerical investigations have validated the effectiveness of this technique. For example, Schiller [7] conducted a detailed experimental campaign on hovering, fixed–pitch propellers, showing that appropriate phase offsets between rotor pairs can reduce the sound pressure level (SPL) at the blade passage frequency (BPF) by more than 5 dB. The research also showed that counter–rotating and co–rotating rotor pairs exhibit

* Corresponding author.
E-mail addresses: francesco.sessini@studio.unibo.it (F. Sessini), diego.donnini@studio.unibo.it (D. Donnini), aldo.chella@studio.unibo.it (A. Chella), thorsten.schwarz@dlr.de (T. Schwarz), jianping.yin@dlr.de (J. Yin), gabriele.bellani@unibo.it (G. Bellani), emanuele.deangelis4@unibo.it (E.L. de Angelis).

https://doi.org/10.1016/j.ast.2026.111699
Received 6 October 2025; Received in revised form 17 December 2025; Accepted 11 January 2026
Available online 15 January 2026

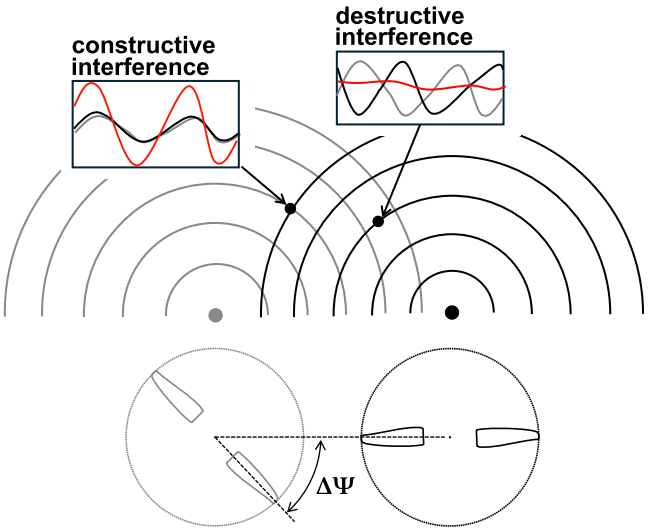

Fig. 1. Schematic illustration of the phase shift concept: Synchronized rotors are coherent sound sources producing sound waves with a phase dependent on their relative blade angular position. The superposition of waves can either increase or diminish noise depending on the observer position.

different noise directivity patterns, with corotating pairs generally allowing for more uniform noise minimization. Following this, various authors explored the sensitivity and broader applicability of phase control. Pascioni [8] modeled its effectiveness in distributed propulsion systems, such as tilt–wing aircraft, showing potential SPL reductions of up to 30 dB in a flyover. However these benefits were found to be highly sensitive to deviations in rotor speed and phase angle enforcement. Specifically, a standard deviation of more than 10° in phase or 0.5 % in RPM can significantly degrade noise mitigation. Guan [9] applied a multi–island genetic optimization algorithm to determine optimal phase angles for quadrotors. The simulations suggested that, for an observation plane located 5 m below the vehicle, noise reductions of up to 30 dB could be achieved for a single observation point, with broader forward regions benefiting from reductions up to 12 dB. The study also highlighted the impact of rotor layout on acoustic performance, identifying diamond–shaped configurations as particularly effective. Finally, Smith's researches [10–12] provide a parametric analysis of the method considering the number of rotors and of blades, the rotational speed and the application to forward flight, but do not consider the attitude control and thus trim of the aircraft. In his findings he reported that the effect of forward flight is to diminish the capability of phase shifting at creating large zones of noise cancellation. Taken together with other research groups [13–15], these studies confirm that phase synchronization constitutes a powerful and flexible approach to rotor noise management in eVTOL vehicles. Unlike traditional passive techniques, it does not interfere significantly with flight dynamics or require structural changes, making it especially attractive for its cost and performance effectiveness.

While these studies have provided valuable insights, most have been limited to fixed–pitch propellers. This presents a significant limitation for eVTOL applications, where variable RPM is typically used for thrust control, making phase synchronization impossible to be implemented. The research here presented aims to overcome this limitation by studying noise cancellation strategy via variable pitch propellers, which allows for thrust control without requiring changes in RPM, effectively decoupling phase synchronization from thrust modulation. This approach offers several benefits, including enhanced power efficiency, and increased maneuverability [16–18]. Indeed, by enabling independent blade pitch adjustments, variable pitch systems contribute to extended flight endurance and reduced operational costs, making them particularly well–suited for advanced VTOL applications [19,20].

Table 1
Rotor blade design parameters.

	Original	Upscaled
Diameter	317 mm	2.2 m
Chord at $r/R = 0.75$	24 mm	0.168 m
Tip speed	84.64 m s^{-1}	121 m s^{-1}
Rotational speed	5100 rpm	1050 rpm
BPF	170 Hz	35 Hz
Collective range	–	0° – 20°

1.1. Rationale and approach

This paper will contribute to the existing body of research by introducing a validated numerical framework capable of predicting the effect of phase shift applied to variable pitch rotor systems. This approach helps to fill the gap between previous fixed pitch research and the real world applicability of the phase synchronization methodology by analyzing the effect of rotor synchronization in realistic trimmed conditions.

The main objective is to numerically assess whether it is possible to control the noise directivity pattern of multirotor VTOL aircraft by implementing an optimized phase shift in both hover and forward flight trimmed conditions.

The developed procedure is based upon existing numerical simulation environments, namely UPM: *Unsteady Panel Method* [21] for aerodynamic analysis and APSIM: *Aeroacoustic Prediction System based on Integral Methods* [22] for acoustic processing. A dedicated simulation toolchain couples the mid–fidelity aerodynamic solver with the acoustic propagator, while also accounting for the vehicle trim condition through a flight mechanics module ensuring stability while maintaining phase synchronization. This module couples with the UPM simulation and provides a precise stability assessment that also takes into account the aerodynamic interactions between the rotors. This procedure is sufficiently fast to consent a parametric study of the problem while retaining most of the effects of relevant phenomena, but it still requires a computation time in the order of hours or days for most complex cases.

To further reduce the computation time required by the acoustic simulation of multiple rotors and especially by an optimization procedure where several cases need to be executed, a simplified analytical model was developed. The acoustic emission in this case is represented by a single, rotating point source per rotor blade and does not require an aerodynamic simulation. The ultimate purpose of this tool would be a real time prediction of sound directivity which can run on a flight computer. Its application is currently limited to the hover case. Both tools were validated against a case study from the NASA Langley research center [7], in which an experimental campaign in the anechoic chamber was performed to investigate the phase shift effect on small scale hovering rotors. The results of the validation are reported in Section 3.

Exploiting such methodology, an investigation is conducted on the application of phase shifting to quadrotor and hexarotor configurations of manned–size vehicles in both hover and forward flight conditions. By performing an optimization of rotor phase angles, the aim is to control the noise directivity and reduce the acoustic emission for specified observer locations.

1.2. Geometric configuration and adopted conventions

The rotor geometry adopted in this research is based on the two–bladed CF125 model designed by KDE Direct, the same configuration employed in the experimental campaign conducted in the aforementioned Schiller study [7]. The authors validated the present numerical toolchain against their acoustic measurements, using the same rotor geometry (see Section 3). The blade geometry was reconstructed by scanning the original rotor. The blade mesh was discretized into 16 radial sections and 94 chordwise panels per airfoil, resulting in a total of 1410

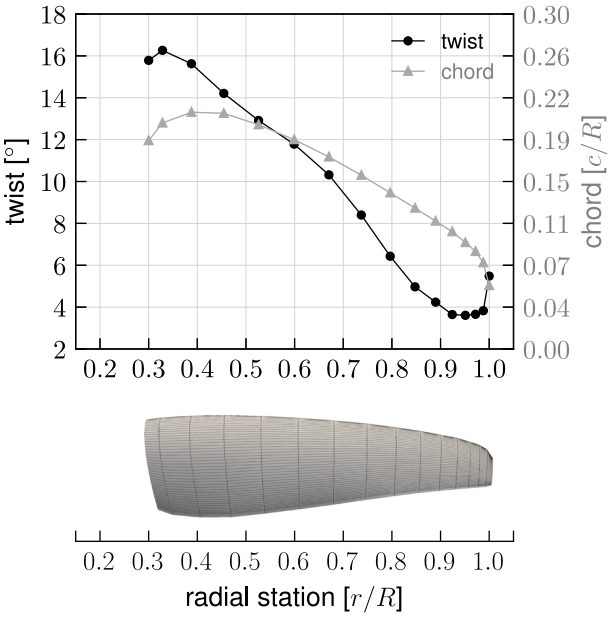

Fig. 2. Radial distributions of the rotor blade chord length and twist (pitch) angle, with a rendering of the blade mesh below. The chord is expressed as a fraction of tip radius.

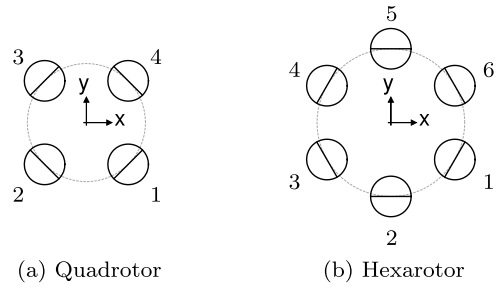

Fig. 3. Parametric rotor layouts.

Table 2
Design parameters of the vehicle configurations.

	Quadrotor	Hexarotor
Weight [kg]	300	450
Tip–tip diameter [m]	4.67	7
Hub–hub distance [m]	3.3	3.5
Rotor diameter [m]	2.2	2.2
Disc loading [N m^{-2}]	193.35	193.35

panels. A root cut–out of 30 % of the radius was introduced to mitigate numerical instabilities in the free–wake solver at low radial stations. Fig. 2 reports the radial distributions of the twist angle and the chord length, and shows a rendering of the resulting mesh. The rotor geometry was then scaled up by a factor of 7 from its original dimensions in order to design a parametric multirotor configuration suitable for a manned–size vehicle. The criterion was to keep the tip speed and the hover thrust coefficient near the values of the fixed–pitch propeller in the experimental study [7], by reducing the angular speed from 534 to 110 rad s^{-1}, ensuring operation within a suitable range of pitch angles and avoiding the onset of stall. Even so, it is inevitable that the up–scaled rotor will not operate under the same design conditions intended by the manufacturer. This is not only due to the different Reynolds number (approximately 10^5 for the original and 10^6 for the up–scaled rotor), but also because the introduction of variable pitch means that geometric and consequently kinematic similarity cannot be maintained. The up–scaled rotor dimensions and characteristics are listed in Table 1. The geometry already has 16° of pitch at the root, and hover is maintained with an additional 3.5° of collective. The panel method UPM includes an approximate boundary layer analysis module, which was used to estimate the hover collective angle leading to stall conditions (through calculation of the shape factor [21]), ensuring to keep a sufficient margin from it in the simulations.

The reference multirotor configuration adopted in this study is the hexarotor layout, designed to mimic the Volocopter 2X [23] overall size and weight. To investigate the influence of rotor number on the phase shift strategy, one additional configuration was considered, featuring 4 rotors. Blade geometry, rotor radius, and rotational speed were kept constant across all setups. In order to maintain a consistent disc loading and comparable pitch attitude in forward flight, the vehicle weight and the approximate fuselage drag model were scaled proportionally with the number of rotors. The main design parameters for the quadrotor and hexarotor configurations are summarized in Table 2, and the corresponding rotor layouts are illustrated in Fig. 3. In all cases, adjacent rotors are counter–rotating to ensure flight controllability. In this paper the analysis focuses only on these configurations, but it is important to note that the entire toolchain is adaptable to any propeller geometry and rotors layout. The preferred flight direction is aligned with the x-axis of Fig. 3, intersecting two rotors. Rotor numbering follows a clockwise sequence, as reported in Fig. 3.

The rotor phase vector $\boldsymbol{\Psi}$, specifies the angular position of each rotor at the start of the simulation. These values are limited to plus or minus half a revolution ($\Psi \in [-90°, +90°]$) because in this case the rotors have two blades spaced 180° apart, and considering higher angles would thus lead to equivalent rotor positions. The Ψ angle obviously changes as the simulation goes forward, but since the rotors have exactly the same angular speed, they remain synchronized. It is thus more straightforward to express the phase as relative to one of the rotors instead of as an absolute value. The convention adopted here is the following: the first rotor is always the reference and thus is set at zero phase in the computation, while we specify the phase difference, or phase shift, $\Delta\Psi$, for all others. A positive angle indicates that the rotor is advanced in its direction of rotation with respect to the first rotor, whereas a negative angle means it is retarded. If we denote the rotor direction with χ equal to $+1$ for counterclockwise and -1 for clockwise rotation, and set the reference rotor at $\Psi = 0°$, then we can define the phase shift as:

$$\Delta\Psi = \chi \cdot (\Psi - 0°), \ \Psi \in [-90°, +90°] \tag{1}$$

and the generic rotor shifted by an angle $\Delta\Psi \in [-90°, +90°]$ will start at:

$$\Psi = \chi \cdot \Delta\Psi \tag{2}$$

with the positive direction of the azimuthal angle Ψ being counterclockwise. A graphical explanation is shown in Fig. 4. Using this convention, the direction of rotation of the reference rotor is not important, and neither is the choice of it, since it is possible to transform the vector to be referenced to any rotor by simply subtracting its phase to all the others.

1.3. Paper layout

After this brief introduction to the problem addressed, the state of the art, and the contribution of this work, Section 2 is dedicated to explaining the methodology behind the simulations performed during the research, including the coupling between the different codes through the toolchain developed by the authors. Section 3 presents the validation process of the numerical tools against the NASA Experimental campaign [7]. In Section 4, the results of the toolchain in hover conditions are reported, with an optimization process based on the analytical method outlined in Section 2.2. Section 5, on the other

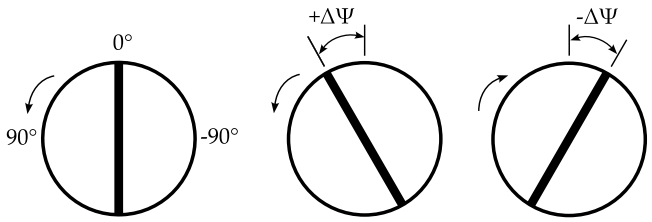

Fig. 4. The blade azimuthal angle Ψ is defined as positive in the counterclockwise direction. The phase difference between rotors is denoted by ΔΨ. On the left, the reference rotor is shown, while on the right, two rotors are displayed with a positive phase shift $\Delta\Psi > 0$, indicating that they are both advanced. Depending on the direction of rotation, the resulting azimuthal angle Ψ will be either positive or negative.

hand, presents the toolchain results in forward flight conditions, optimized with a dedicated numerical procedure. Finally, Section 6 summarizes the conclusions regarding the overall results and future research directions.

2. Methodology

The structure and basic theory behind the numerical simulation and the analytical tool are outlined in the following sections. First, a step-by-step overview of the architecture is presented to provide a general understanding of the contribution of each component in the toolchain. Then, each tool is explained individually, focusing on the most relevant details for this research. For further information on the simulation software from DLR, please refer to [21,22].

2.1. Simulation toolchain

The acoustic signature of the analyzed vehicle is obtained through a two step procedure: the first is the aerodynamic simulation, which provides the flow solution at the blades surface and assumes that the flight condition, the vehicle's attitude and all of the control inputs are known, as well as obviously the vehicle geometry. The result becomes then the input of the acoustic solver, which calculates the sound propagation in the far field. In order to automate the procedure and to study the effect of relevant parameters, such as rotor phase vector, number of rotors, hub to hub distance or flight velocity, without having to manually change inputs each time, a toolchain was implemented through wrapping scripts in Python language. It operates a mid–fidelity panel code (UPM) and an acoustic solver (APSIM), handling the required input and output data for the two programs and performing some post–processing, without requiring user intervention except for the initial settings. A schematic representation of the simulation workflow is depicted in Fig. 5. To reproduce realistic flight condition, a trim procedure which couples with the panel code was developed and constitutes a preliminary step to the whole simulation.

2.1.1. Trim procedure

The multirotor vehicle configuration is numerically trimmed by a Python script, which couples with the aerodynamic solver UPM in an iterative procedure in order to find the trim variables. We refer here to the hexarotor configuration as the example, but an analogous procedure applies also to the quadrotor described in the introduction. The possible steady flight conditions considered are hover, level forward flight and steady climb or descent. Due to the symmetry of those conditions, a first approach was to limit the control to 3 degrees of freedom (DoF), considering only the surging, heaving and pitching motions. This proved to be satisfactory for the forward flight condition while greatly improving the computational time. This brief explanation is limited to this implementation. However, a 6 DoF procedure was also developed

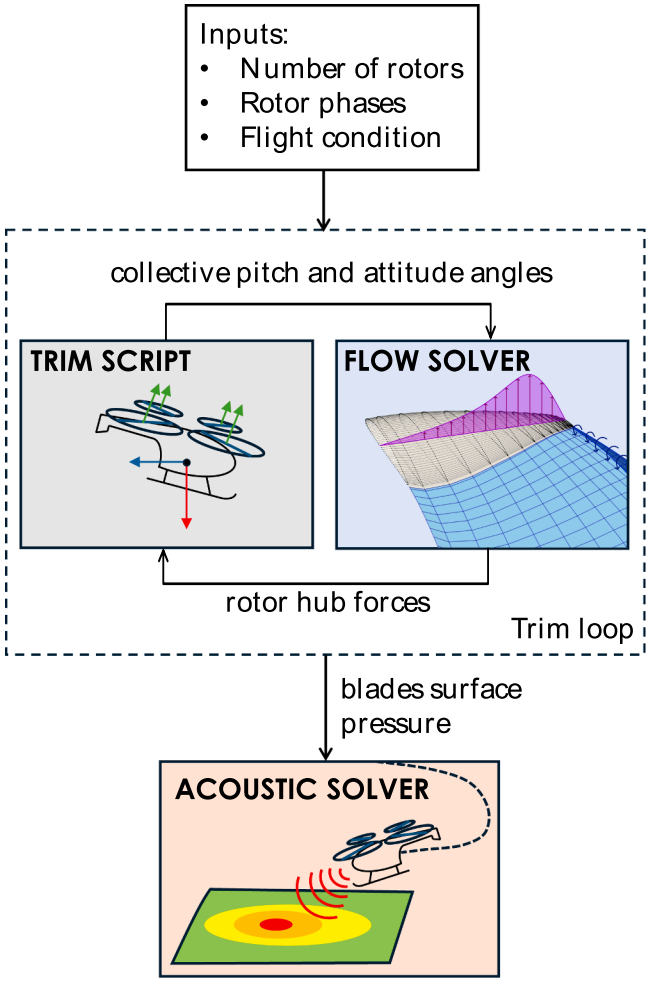

Fig. 5. Block diagram of the simulation toolchain.

and used for the hover case, where thrust asymmetries due to aerodynamic interaction influenced the rotors pitch setting. Surge and heave motions are given by translational dynamics in x and z directions respectively, and pitching motion is determined by rotational dynamics around the y axis. The vector containing the corresponding forces and moments is expressed in a local horizontal reference system, which is parallel to the inertial one but fixed to the vehicle center of gravity, and is termed $\boldsymbol{y} = [F_x, F_z, M_y]^T$. Those components are evaluated by averaging the aerodynamic forces acting on the rotors, provided by the UPM computation for each time step, over one rotation, and are then completed by the vehicle weight force and the drag of rotor booms and fuselage, which was estimated with a simplified model. The resultant longitudinal forces are the rotor thrust and drag (so called *H–force*), respectively perpendicular and parallel to the rotor plane, the fuselage drag applied to the center of pressure and parallel to the wind direction, and the rotor booms drag applied to the rotors plane geometric center. The drag produced by the rotors induces a pitch up moment, instead the fuselage drag creates an opposite pitch down moment, since the center of gravity is estimated between the rotors plane and the fuselage center of pressure. Other smaller sources of moments come from the rotor hubs as calculated by UPM due to lift dissymmetry in forward flight.

The objective of the trim is to make all $\boldsymbol{y}$ components equal to zero or as close to it as possible. The so called trim vector $\boldsymbol{x}$ must also contain 3 components in order for the problem to be solvable. A mapping matrix is employed to correlate it to the control inputs, which are the six collective pitch angles θ_o^i of the rotors, and to the attitude pitch (or elevation) angle Θ, which are the unknowns of the equilibrium problem. The mapping

matrix is in this case:

$$\begin{bmatrix} \theta_o^1 \\ \theta_o^2 \\ \theta_o^3 \\ \theta_o^4 \\ \theta_o^5 \\ \theta_o^6 \\ \Theta \end{bmatrix} = \begin{bmatrix} -1 & 1 & 0 \\ 0 & 1 & 0 \\ 1 & 1 & 0 \\ 1 & 1 & 0 \\ 0 & 1 & 0 \\ -1 & 1 & 0 \\ 0 & 0 & -1 \end{bmatrix} \cdot \begin{bmatrix} x_1 \\ x_2 \\ x_3 \end{bmatrix} \tag{3}$$

The problem is then solved numerically for $\boldsymbol{x}$ by means of a Newton–Raphson iterative algorithm, approximating the Jacobian matrix with finite differences. Before the trim iteration, a UPM computation is performed automatically for a number of rotor revolutions sufficient to achieve a developed wake and converged rotor thrust. This serves as a basis for the subsequent computations which are restarted from it. Then the trim loop begins: the Jacobian matrix is computed by running one simulation revolution with a step input of each trim variable, then the approximate solution of the input vector is used to compute the new control variables and restart another revolution to compute the actual value of $\boldsymbol{y}$. If its norm is less than the tolerance the iteration is stopped.

The trim procedure was tested using the same convergence criteria based on residual forces and accelerations as defined by Volocopter [23]. Furthermore, a robustness analysis of the methodology was carried out against the forward speed, considering a level forward flight condition. The objective was to identify the velocity threshold beyond which the loads computation instabilities of the aft rotors, disturbed by the wake interaction from the front ones, compromise the procedure from fully converging.

2.1.2. Aerodynamic solver: UPM

Once the trim procedure is complete, the collective pitch angle for each rotor θ_o^i and the elevation angle Θ are used as input for the UPM aerodynamic simulation of the multirotor in the prescribed steady flight condition. The Unsteady Panel Method UPM [21] is a mid–fidelity aerodynamic simulation tool, capable of treating flows around complex three dimensional configurations in combination with a non–linear unsteady free wake. The code was originally developed for rotorcraft applications and can be used to evaluate the interaction of the main rotor wake with the tail rotor as well as with the fuselage and empennages. Its versatility allows for the implementation of multiple lifting rotors, which is the case of the present work. It is particularly suitable for such a study since it is capable of capturing many of the important features which influence sound generation in rotors (steady and unsteady loading, blade–vortex and rotor–wake interaction, blade geometry) while requiring a lowered computational cost. Higher fidelity CFD methods would render highly impractical a parametric study with more than two rotors involved.

UPM is based over a potential flow formulation, in which a superposition of singularities, placed on three–dimensional panels as shown in Fig. 6, is used to build the generic solution to the flowfield. Lifting surfaces (rotor blades) are modeled by:

- a source/sink distribution on the surface to simulate the displacement of the flow.
- a surface with bound circulation (given by constant strength doublet panels) inside the blade (corresponding to the mean camber surface) to model the lift.
- a short zero–thickness elongation of the trailing edge along its bisector, called the Kutta panel, on which the Kutta condition of tangential flow at the trailing edge is applied.

At the start of any simulation, no wake is present and rotors (or wings) are impulsively set in motion. Then at each time–step (specified as degrees of rotor rotation) a row of wake panels is shed from the Kutta panel of each blade, consisting of vortex rings (constant strength doublet panels) with a fixed amount of circulation. Due to the unsteadiness of the flow, an additional condition, other than flow tangency, is imposed to equalize pressures on the two sides of the trailing edge, called the *pressure Kutta condition*, which requires an iterative solution. A free–wake is progressively made up by a mesh of trailed and shed vorticity lines, with the position of each node being calculated at each step considering the induced velocity from the blades and the wake itself. The pressure distribution on the blades is calculated from the velocity field with the unsteady Bernoulli equation and is then used as input for the aeroacoustic solver.

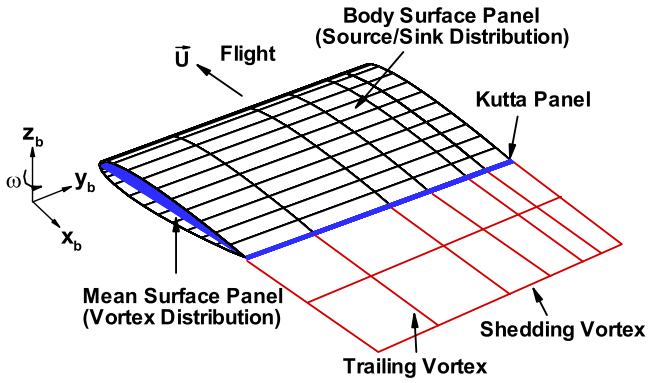

Fig. 6. Numerical model of the blade and the wake from Kunze [21]. Each wake panel is a constant doublet distribution, which is equivalent to a vortex ring of constant strength. The difference in circulation between adjacent panel edges forms lines of vorticity which we refer to as streamwise trailed vorticity and spanwise shed vorticity.

2.1.3. Aeroacoustic solver: APSIM

The Aeroacoustic Prediction System based on an Integral Method APSIM [22] is a numerical tool for the prediction of rotor or propeller noise radiation in the free far–field. It is based over the Ffowcs William–Hawkings acoustic analogy and only linear sound propagation is taken into account. In this work, the solid surface formulation of the wave equations was employed, which requires the geometry and kinematics of the blades together with the pressure distribution, across one rotor revolution. This approach neglects sound generated by viscous phenomena and considers only the tonal sources related to displacement of fluid by the blade (thickness noise) and the rotation of the blade pressure field (loading noise). In particular, aeroacoustic sources are distributed on the blade mesh in form of monopoles and dipoles, respectively generating thickness and loading noise, with given strength dependent on the solution from the aerodynamic solver.

The calculation of the acoustic pressure time series is performed over a specified grid of measurement points (*microphones*), in particular a hemisphere centered around the vehicle is used to measure the radiated sound power and the polar sound directivity, together with a rectangular plane under the vehicle capturing the noise footprint on ground. The microphone grid is specified in the same reference system as the blade motion. This means that relative motion between the ground and the vehicle is not considered and doppler effect caused by it is neglected.[1] The effects of ground reflection and of atmospheric absorption were neglected as well in the current work. The acoustic simulation performed by the toolchain is divided in two main parts: the computation of sound emission (or better of the estimation) for the non synchronized configuration, and the complete simulation which considers the effective synchronization of rotors and computes the sound sources all at once. To estimate the noise emission of a configuration of rotors equivalent to the one considered in the aerodynamic simulation but with uncontrolled phase relation between rotors, two assumptions were made:

[1] Note that the effect of the moving flow on sound propagation is taken into account by the program.

- the phase of each rotor is random. This is what generally happens with rpm control of motors: the controller follows the speed set point but does not track the relative phase.
- the rotor–to–rotor and rotor–to–wake aerodynamic interferences are weakly dependent on the rotor relative phasing.

As a consequence the total acoustic emission was calculated summing on a linear energy basis, which is equivalent to summing in the frequency domain, the acoustic pressures generated by each rotor. Operatively, the script isolates each rotor pressure data and performs a separate acoustic simulation, then the squared rms value of the acoustic pressure in each grid node is summed between all rotors. The output is the SPL distribution on the considered grid, representing the baseline to which we can compare the effect of rotor phase synchronization.

Next, the complete simulation is computed from the unaltered pressure files from UPM, for the specified microphone grids. From the time series of the acoustic pressure $p'(t)$ we can perform a Fourier analysis and obtain the SPL (sound pressure level) distribution across frequencies. The overall SPL is then obtained integrating across the entire frequency spectrum or equivalently by calculating the root mean square value of the pressure fluctuation:

$$SPL = 20\log\left(\frac{p_{rms}}{p_o}\right), p_o = 2\cdot 10^{-5}\ \text{Pa} \tag{4}$$

For the entirety of the paper, the shown SPL values will always refer to the overall SPL calculated with the above formula unless otherwise specified.

2.2. Analytical model

An analytical model was developed to provide a simplified and faster tool for the prediction of the acoustic far–field of multirotor configurations. While it obviously lacks in accuracy, it is considerably lighter in computational cost, which renders it useful for iterative optimization studies such as the one presented in this work. Another interesting application would be the implementation of the model onboard of a flight computer for in–flight prediction of acoustics. Its current version is limited to hovering flight.

The model is based on the Ffowcs Williams–Hawkings (FW–H) acoustic analogy and specifically on Farassat's Formulation 1A equations, which are the same used by the APSIM software explained in Section 2.1.3. The difference is that while those equations, due to their integral formulation, are normally solved over a surface mesh, here they have been simplified by compacting the noise sources: each rotor blade's acoustic emission is represented as a single point source located at its tip. This point–source approach is based on the formulation described by Delfs [24], which provides explicit equations for the pressure contributions from two fundamental types of noise sources:

- monopole source: models the thickness noise, representing the displacement of the fluid by the blade's volume.
- dipole source: models the loading noise, which results from the aerodynamic forces (lift and drag) acting on the blade.

This approach intentionally neglects the distributed nature of the acoustic sources along the blade span and chord, as well as the nonlinear quadrupole sources, which are considered secondary for the subsonic tip speeds under investigation.

The validity of this point-source representation relies on the compact source assumption, quantified by the Helmholtz number:

$$He = \frac{2\pi l}{\lambda} \tag{5}$$

where l is a characteristic source dimension and λ is the acoustic wavelength. For $He \ll 1$, the source is acoustically compact and can be reasonably approximated with a point source. Considering the blade chord at 75% radius as the characteristic length and the blade passage frequency ($c_{75} = 0.168$ m, BPF = 35 Hz for the upscaled rotor), the Helmholtz number is approximately 0.11, remaining below unity up to the 8th harmonic. Since rotor tonal noise energy is predominantly concentrated in the lower harmonics, this assumption is appropriate for the directivity optimization objective of this study.

Using this approach it is not necessary to calculate the pressure field across the entire blade surface and it is sufficient to estimate the magnitude of the lift vector. Furthermore, the model does not account for the complex aerodynamic interactions between rotors, assuming that the acoustic field is a linear superposition of the sound generated by each rotor operating in isolation.

The pressure fluctuation, $p'(x,t)$, will then be given by the sum of two components: thickness noise (monopole) and loading noise (dipole). The thickness noise component is calculated as:

$$p'_{\text{thick}}(x,t) = \frac{1}{4\pi}\left[\frac{\frac{\partial\theta_p}{\partial\tau} + \boldsymbol{e}_R\cdot\frac{\partial \boldsymbol{M}_q}{\partial\tau}(1-M_{qR})^{-1}\theta_p}{R_i(1-M_{qR})^2} + \frac{a_\infty(M_{qR}-M_q^2)\theta_p}{R_i^2(1-M_{qR})^3}\right]_{\text{ret}} \tag{6}$$

The loading noise component is given by:

$$p'_{\text{load}}(x,t) = \frac{1}{4\pi}\left[\frac{\frac{\partial \boldsymbol{f}_p}{\partial\tau}\cdot\boldsymbol{e}_R + (\boldsymbol{f}_p\cdot\boldsymbol{e}_R)\frac{\partial \boldsymbol{M}_q}{\partial\tau}\cdot\boldsymbol{e}_R(1-M_{qR})^{-1}}{a_\infty R_i(1-M_{qR})^2} + \frac{-\boldsymbol{f}_p\cdot\boldsymbol{M}_q + (1-M_q^2)(\boldsymbol{f}_p\cdot\boldsymbol{e}_R)(1-M_{qR})^{-1}}{R_i^2(1-M_{qR})^2}\right]_{\text{ret}} \tag{7}$$

where:

- $[\cdot]_{\text{ret}}$ indicates evaluation at the retarded time (i.e. the emission time), τ.
- θ_p is the mass source strength [kg s^{-1}].
- $\partial/\partial\tau$ is the source–time derivative.
- R_i is the source–observer distance.
- $\boldsymbol{e}_R$ is the radiation direction unit vector.
- $\boldsymbol{M}_q$ is the source Mach vector, and $M_{qR} = \boldsymbol{M}_q\cdot\boldsymbol{e}_R$.
- a_∞ is the far–field speed of sound.
- $\boldsymbol{f}_p$ is the point force vector [N].

The mass source strength, representing the thickness noise contribution, is approximated from the mass flow displaced by the rotating blade over one revolution. The blade is modeled as a rectangular planform with uniform thickness, yielding:

$$\theta_p = \frac{\omega(R_t^2 - R_h^2)\,t_b}{2} \tag{8}$$

where R_t is the blade tip radius, R_h is the hub (root cutout) radius, t_b is the blade maximum thickness, and ω is the angular velocity. This formulation represents a first-order approximation of the volume displacement rate, consistent with the compact source assumption discussed before in this section. More rigorous approaches in the literature express the monopole source strength as a function of the blade cross-sectional area integrated along the span [25], but this level of detail was valuated unnecessary at the moment for the directivity-focused optimization objective of the present work. The point force vector $\mathbf{f}_p$, representing the loading noise contribution, is derived from the blade lift. For the hover condition this was straightforward to estimate.

The Python implementation employs a systematic procedural workflow structured around three key computational phases. Initially, the algorithm defines the geometric configuration of the multirotor system and establishes a spatial grid of virtual microphones serving as acoustic observers. Subsequently, for each blade tip acting as a noise source and corresponding microphone position, the model computes the source's temporal trajectory and associated kinematic parameters. The computational framework utilizes a generalized coordinate system (as illustrated in Fig. 7) where the global origin is positioned offset from each rotor's center while maintaining coplanarity. This design enables seamless adaptation to arbitrary multirotor configurations through procedural geometry generation. The constant radial distance from the global

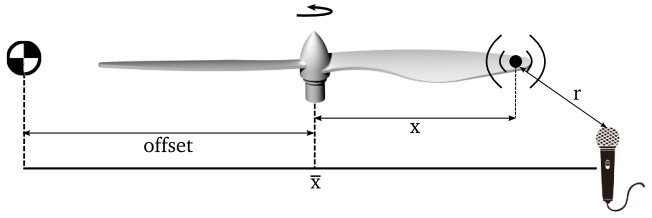

Fig. 7. Geometrical representation of the rotor and virtual microphones. Notation: $[\bar{x}, \bar{y}, \bar{z}]$ are microphone coordinates; $[\text{offset}_x, \text{offset}_y, \text{offset}_z]$ are rotor center coordinates; $[r_x, r_y, r_z]$ are blade tip coordinates relative to microphones.

origin to each rotor center is designated as the "offset" parameter, while microphone coordinates relative to this origin are denoted with overbar notation as $[\bar{x}, \bar{y}, \bar{z}]$.

The position of each blade tip source evolves according to circular motion kinematics, with coordinates defined relative to the rotor center as:

$$\begin{cases} x = r\cos(\theta_s + \omega\tau + \Psi) \\ y = r\sin(\theta_s + \omega\tau + \Psi) \\ z = 0 \end{cases} \tag{9}$$

where r is the rotor radius, θ_s represents the initial blade angular position (e.g., 0° and 180° for a two–blade rotor measured from the positive x-axis), ω is the angular velocity, τ is the emission time, and Ψ accounts for phase shifts between multiple rotors. The distance vector from each source to a fixed microphone is computed as:

$$\boldsymbol{R}_{\text{obs}} = \begin{bmatrix} \bar{x} - x - \text{offset}_x \\ \bar{y} - y - \text{offset}_y \\ \bar{z} - z - \text{offset}z \end{bmatrix} \tag{10}$$

A critical aspect of the acoustic modeling involves determining the emission time τ, which accounts for the finite propagation speed of sound from moving sources. Since the source position depends on the emission time itself, this creates an implicit relationship that must be solved iteratively:

$$t = \tau + \frac{|\boldsymbol{x}_{\text{obs}} - \boldsymbol{y}_{\text{src}}(\tau)|}{c_0} \tag{11}$$

where t is the observer time, $\boldsymbol{x}_{\text{obs}}$ and $\boldsymbol{y}_{\text{src}}$ represent the observer and source positions respectively (with $\boldsymbol{y}_{\text{src}} = \boldsymbol{x} + \textbf{offset}$), and c_0 is the speed of sound. This nonlinear equation is solved numerically using the Newton–Raphson method to determine the emission time for each source–observer pair at each time step. Once the emission time is known, the time–domain pressure fluctuation $p'(x,t)$ is calculated using Eqs. (6) and (7). The total acoustic pressure at an observer is then determined by the linear superposition of the pressure fluctuations from all blades on all rotors, carefully accounting for the user–defined phase shift, Ψ_i, for each rotor. Finally, the Sound Pressure Level (SPL) is computed from the root mean square of the predicted pressure time series (Eq. (4)) over the final rotor revolution.

The model was validated against experimental data from the NASA Langley Research Center [7] and against the higher–fidelity APSIM solver. The validation process, reported in Section 3, confirmed that, despite its simplifications, the model successfully captures the fundamental directivity patterns and the relative changes in the acoustic field due to rotor phasing, while the absolute magnitude of the predicted SPL can be less accurate. Its primary role within this research is to serve as a fast cost function for an optimization algorithm, used to calculate optimal phase angles in hover that can then be verified and analyzed in more detail using the complete UPM–APSIM toolchain.

3. Validation of the method with experimental data

The simulation toolchain applied to hovering, fixed-pitch propellers was validated with the experimental data presented by NASA research scientist N. Schiller in his work *"Tonal noise control using rotor phase synchronization"* [7]. In his experimental campaign on phase control of fixed pitch propellers he investigated the possibility of altering the tonal noise signature of a double rotor configuration in the hover condition.

The experimental case was reproduced with the methodology presented in Chapter Section 2 and the results are reported in what follows. The aim of the validation was establishing if the influence of rotor phasing and rotor-to-rotor interactions on the magnitude and directionality of the noise signature was correctly captured by the numerical toolchain, while with respect to the analytical model the focus was mainly around sound directivity.

3.1. Description of the NASA experimental setup

The experiments where performed in the NASA Langley Structural Acoustic Loads and Transmission (SALT) anechoic chamber on a static dual rotor assembly. Both clockwise and counter–clockwise two–bladed propellers were used depending on the test case. A detailed description of the blade geometry has been given in Section 1.2 (Table 1). Hub-to-hub separation is 400 mm, which corresponds to 1.26 times the rotor diameter and gives a tip clearance of 83 mm. Each hub attaches to a short shaft placing the rotor plane at a distance of 59 mm from the horizontal support arm. Both shafts are connected to a single brushless DC motor by means of a belt and pulleys, in this way the rotation is synchronized and the relative phase offset is mechanically fixed. The rotor assembly is mounted on a rotating stage on top of a test stand which located it in the center of the anechoic chamber. The propeller speed was set to $5100rpm$ corresponding to a blade passing frequency (BPF) of 170 Hz.

For the acoustic measurements, five free-field microphones were placed at a radial distance of 1.9 m from the center of the test bench, all on the same azimuthal angle starting at 0° elevation angle and going down to −11.25°, −22.5°, −33.75° and −45°. Keeping the microphone array stationary, the test bench was rotated to take the measurements for a total of 31 different azimuthal angles in 11.25° steps, in order to capture the sound directivity on a portion of the hemisphere, as shown in Fig. 8a. The direction of rotation of the rotors is described as seen from above, and a right handed reference system is placed with the origin in the mid point between the rotors, resting on the rotors plane, with the x axis pointing to the front of the rotors and the y axis pointing to the left hand propeller, as can be seen in Fig. 8b. The azimuthal angle is considered 0 at the x axis and positive counter–clockwise.

3.2. Results comparison

A total of six test cases were considered in the experimental campaign and were reproduced numerically in this work. The test matrix is displayed in Table 3. The output of the experiment were the pressure time histories over the measurement points. From them it is possible to calculate the acoustic spectra using an FFT algorithm. Since the study [7] was focused on tonal noise corresponding to the BPF, the sound pressure level (SPL) was calculated from measured data by integrating the spectrum over an interval of 10 Hz centered around said frequency. The reason is flow recirculation in the test room, which influences the harmonic content of rotor noise due to the wake being ingested and causing unsteady loading events. To isolate the steady loading noise source the integration around the BPF was performed as described. It is important to stress that for all numerical results presented in this paper, the SPL was instead obtained through direct calculation of the root mean square of the pressure fluctuation, as in Eq. (4), thus encompassing all frequencies.

The reported results were the overall sound pressure level distribution around the azimuth (SPL polars) at two elevations of the

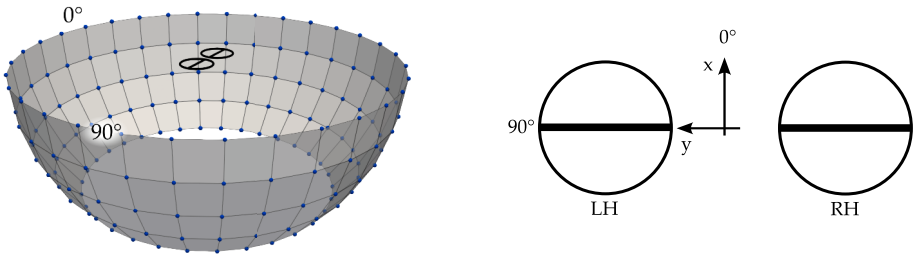

(a) Grid of microphone points (blue) and panels (grey) used for the integration of sound intensity, around the double-rotor configuration.

(b) Reference system, view from above.

Fig. 8. Scheme of the NASA experimental setup.

Table 3
Test cases matrix. Rotors viewed from above, left hand rotor stands on the left.

Testcase	Phase shift	Scheme
Single ccw	n/a	
Counter–rotating	0°	
Counter–rotating	90°	
Co–rotating	0°	
Co–rotating	45°	
Co–rotating	90°	

Table 4
UPM simulation parameters for the experimental case study.

UPM parameters	
time step size	6°
number of revolutions	16
vortex core radius	$0.8 \cdot c_{75}$
environment	SL 23°C
wake size	unrestricted

hemisphere, which show the noise directivity, plus the radiated power over the measurement hemisphere. A simulation was performed with both the numerical toolchain and the analytical model for each test case, and results are compared in the next sections. The relevant input parameters regarding the mid-fidelity flow solver are reported in Table 4.

3.2.1. Polar distribution of sound pressure level

The main result of the experiment were the polar plots of the sound pressure level over two elevations of the hemisphere. In Fig. 9 we can compare the experimental data with the numerical toolchain and the analytical model, for the hemisphere slice located at an angle of −45° under the rotors plane and four out of the six testcases which were deemed most relevant.

The simulation results closely match the experimental data, and the figure presents testcases were the highest discrepancy is found. It has to be noted that, in the regions far under the rotors plane, a higher scatter is present in the measurements, as evidenced in the article [7]. The analytical model is able to capture the directivity of sound (meaning the shape of the polar plot) quite well.

The magnitude of SPL is not far off either, but it must be noted that it strongly depends on two input parameters: the mass source strength θ_p and the point force $\mathbf{f}_p$. In the present analytical model, these quantities are estimated using simplified approximations suitable for a preliminary assessment of noise , as showed in Section 2.2. In particular, the mass source strength θ_p in Eq. (8) was calibrated against the available experimental data in this validation stage. This tuning approach was adopted for the present work to obtain reliable results despite the simplified modeling of the mass source. Future developments should focus on improving the a priori prediction of θ_p from blade geometry alone, potentially through more detailed modeling of the blade thickness distribution or adoption of the compact-form formulations available in the literature. [25]

The region under the rotors is dominated by the loading noise, which radiates mainly out of plane, contrary to thickness noise sources which emit in the plane. During hovering, thickness noise is the major source and we find that SPL levels get lower as we go down the hemisphere, but this changes quickly when transitioning to forward flight. Sound radiation from an hovering, isolated propeller is uniform over the azimuth, is maximum in the rotor's plane and diminishes under it, as discussed above. The radiation in-plane is similar to that of a still monopole source.[2]

When two rotors are corotating in phase ($\Delta\Psi = 0°$) they also emit as a still monopole (in-plane) with an SPL increase of nearly 6 dB, which would be the theoretical difference for two coincident in-phase monopoles. This is almost true also out-of-plane, as shown in Fig. 9a, with the emission being slightly skewed. The reason is the compactness of the sound source, in this case the two rotors, which allows for sound waves to be nearly in-phase for all emission angles. The greatest SPL reduction averaged around the azimuth is obtained when the phase shift is set at 90° for the corotating propellers, creating an 8-shaped emission pattern which resembles the one of a still dipole, see Fig. 9b. We remind that a dipole source is obtained superimposing a monopole with another one of equal intensity but completely out of phase.[2]

In the case of counter–rotating rotors, the distance between propeller blades, and thus of sound sources, is constantly modulated during one rotation. A different pattern is created with local maxima, where sound waves are in-sync and thus form constructive interference, and local minima, where sound waves nearly perfectly cancel out due to destructive interference. The resulting sound directivity forms a characteristic quadruple lobe shape,[2] as can be seen in Fig. 9c and d. Those lobes can apparently be rotated, up to a certain amount, by tuning the phase shift, without affecting much their shape or amplitude. This was the first inspiration to the work presented in this

[2] See Rienstra and Hirschberg [26] for an in depth discussion on the radiation pattern of acoustic sources.

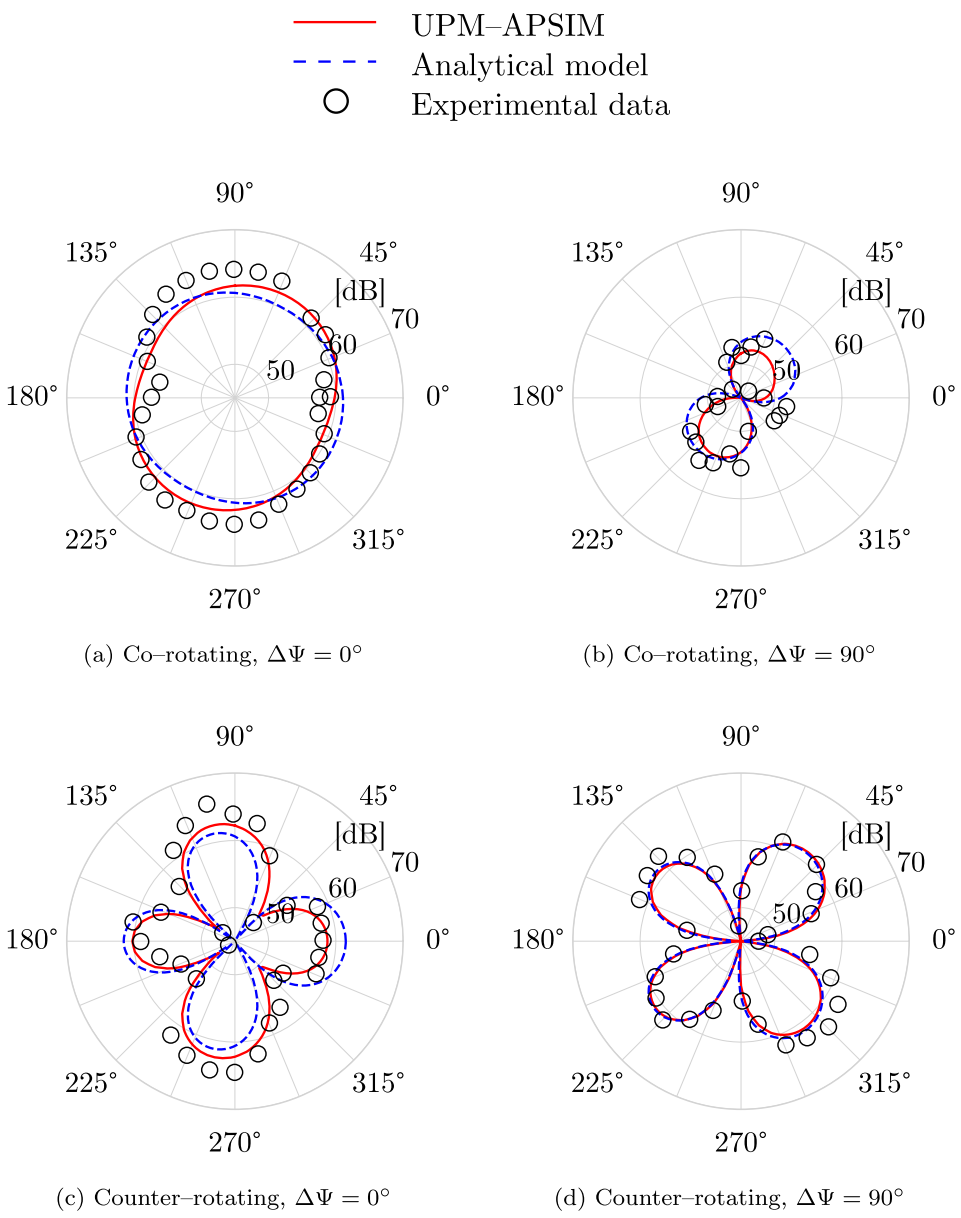

(a) Co–rotating, $\Delta\Psi = 0°$ (b) Co–rotating, $\Delta\Psi = 90°$

(c) Counter–rotating, $\Delta\Psi = 0°$ (d) Counter–rotating, $\Delta\Psi = 90°$

Fig. 9. Sound pressure level in [dB], plotted as a polar line against the azimuthal angle, at an elevation angle of −45° thus out and under the rotors plane (lowest row in microphones grid of Fig. 8a). The values predicted by the numerical simulation toolchain (solid red line) and the analytical model (dotted blue line) are compared to the experimental data (black circles, NASA [7]) for four out of the six test cases of Table 3. (For interpretation of the references to colour in this figure legend, the reader is referred to the web version of this article.)

research, raising the question of whether it was possible, and to what extent, to exploit this directional control with more rotors in real flight maneuvers.

3.2.2. Radiated sound power

To evaluate the sound power radiated through the hemisphere, the measurement grid was considered to be in the far-field and thus the approximation of locally planar wave front was employed. Then the sound intensity has only a radial component and is approximated by the squared rms pressure over the speed of sound times air density. The radiated power is then obtained by multiplying the value of sound intensity at each local hemisphere panel with its area and summing up the results. This procedure was followed in [7] and was replicated for the UPM-APSIM results. The analytical model was not considered since the estimation of absolute noise magnitude was not its designed purpose.

The sound power value is normalized w.r.t. double the one of the isolated rotor, obtaining a difference of sound power level as seen below:

$$\Delta PWL = 10 \log \left(\frac{P}{2P_{single}} \right) [\text{dB}] \tag{12}$$

A positive value means an increase of radiated sound power with respect to an unsynchronized double propeller configuration, a negative value on the contrary means that a reduction has been achieved, a value of 0 represents no change. Results are reported in Table 5.

Due to the way the data is normalized, the single rotor value is −3 dB, or 3 dB under the baseline, since the radiated power is exactly half of the reference. The counter–rotating case does not cause great deviation from the reference, which means that zones where sound is attenuated are balanced by others where it is increased. The co-rotating rotors increase the value by 2.5 dB when they are in phase and instead decrease it by almost 6 dB when they are shifted by 90°, which means that the sound power was reduced by almost three quarters.

Table 5
Radiated sound power level [dB] normalized with double the power radiated by single propeller, comparison between NASA experimental values [7] and numerical simulation results.

Configuration	experimental	numerical (APSIM)
single propeller	−3.0	−3.0
counter–rotating, $\Delta\Psi = 0°$	+0.4	+0.2
counter–rotating, $\Delta\Psi = 90°$	−0.3	+0.1
co–rotating, $\Delta\Psi = 0°$	+2.5	+2.5
co–rotating, $\Delta\Psi = 45°$	−0.2	0.0
co–rotating, $\Delta\Psi = 90°$	−5.8	−5.6

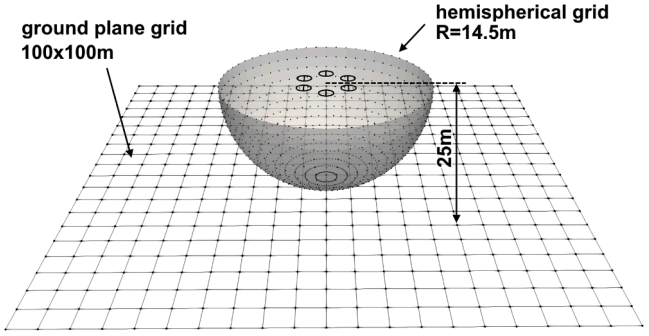

Fig. 10. Acoustic simulation domain for the hover case. The multirotor is centered over a square ground plane, at a height of 25 m and inside a hemispherical microphone grid.

4. Application to hovering flight

In this section we present the application of the simulation methodology to the quadrotor and hexarotor configurations, as described in Section 1.2, in the hovering condition. The aim was to adjust rotor phase angles to control the noise footprint and achieve local minima in the overall sound pressure level within targeted ground regions. An optimization was performed using the analytical model, and the optimized phase angles were the input for the complete aeroacoustic simulation.

4.1. Simulation setting

The vehicle is considered at an altitude of 25 m above the ground, which is represented by a square plane of 100×100 m, in accordance with the EASA guidelines on environmental protection for the new VTOL generation [27]. The trimmed flight condition and the simulation parameters are reported in Table 6. The wake in hover is unrestricted. The computational domain is illustrated in Fig. 10. A far–field hemisphere with a radius of 14.5 m, centered around the aircraft, was also used. Its purpose is to assess the overall sound directivity and to calculate the radiated sound power. To enable the optimizer to focus on specific directions, both the hemisphere and the ground plane were partitioned into nine distinct sections, each spanning 40° degrees. This partitioning allows the optimization to focus its efforts on minimizing noise in a specific direction relative to the aircraft's frame (e.g., forward, sideways, or rearward). Within each target section, a grid of virtual microphones was defined to sample the acoustic field. The objective of the optimization was to minimize the noise within one of these user–selected sections.

4.2. Optimization procedure

The analytical model, described in Section 2.2, provides a computationally efficient means to predict the acoustic field, making it suitable for an optimization routine aimed at finding optimal rotor phase angles. Due to the complex, nonlinear, and often multi–modal nature of the acoustic interference problem, a gradient–based optimization approach is not effective and instead a stochastic, global search method is required. For this purpose, a Real–Coded Genetic Algorithm (RCGA) was implemented [28].

Table 6
Parameters for the hover test case.

Flight parameters	
Flight condition	Hover
$\|\|\mathbf{TAS}\|\|$	0 m s^{-1}
Advance ratio μ	0.00
Tip Mach number M_t	0.35
Environment	25 m ISA +8 °C
UPM parameters	
Time step size	6°
Number of revolutions	12
Vortex core radius[a]	$0.8 \cdot c_{75}$
Wake size	Unrestricted

[a] c_{75} refers to the chord length at 75% of the rotor radius.

4.2.1. Problem formulation

The optimization problem is defined as follows: for a multirotor aircraft with N rotors, the goal is to find a set of phase angles that minimizes the noise in a predefined target region.

- Design Variables: The variables for the optimization are the phase angles of $N-1$ rotors. As explained in Section 1.2, the first rotor is the reference with a fixed phase of 0°, and the phase shift angle $\Delta\Psi_i$ for each subsequent i^{th} rotor is allowed to vary within the range $[-90°, +90°]$. The solution is represented by the vector: $\Delta\boldsymbol{\Psi} = [\Delta\Psi_2, \Delta\Psi_3, \ldots, \Delta\Psi_N]$. The number of possible phase combinations is given by:

$$\left(\frac{360°}{\delta\Psi \cdot N_b}\right)^{N-1} \tag{13}$$

  in which $\delta\Psi$ is the chosen angular resolution in degrees, N_b is the number of blades and N the number of rotors.
- Objective Function: The cost (or fitness) of a given phase vector $\Delta\boldsymbol{\Psi}$ is the mean Sound Pressure Level (SPL) calculated over the discrete set of microphone locations within the designated target section:

$$\min\left(\frac{1}{N_{obs}}\sum_{i=1}^{N_{obs}} SPL_i\right) \tag{14}$$

  in which N_{obs} is the number of observers (microphones or grid points) in the target region.
- Constraints: The optimization is constrained by the lower and upper bounds imposed on the phase angle variables.

As said, the aim was to find the set of phases which would produce a local minimum of SPL in the desired region. The optimization procedure, which analyzes only the specified set of observers and not the entire plane, looks for the absolute minimum described by Eq. (14) with respect to the variable space given by the phase angles. It is thus important to underline that the mean value of SPL in the minimized region may not be the absolute minimum of the entire observation plane but only a local one.

4.2.2. Genetic algorithm

The RCGA operates iteratively through the following steps:

1. Initialization: An initial population of candidate solutions (vectors of phase angles) is generated randomly within the defined bounds.
2. Evaluation: The fitness of each candidate solution is evaluated by computing its cost using the analytical model. A lower mean SPL corresponds to a higher fitness.

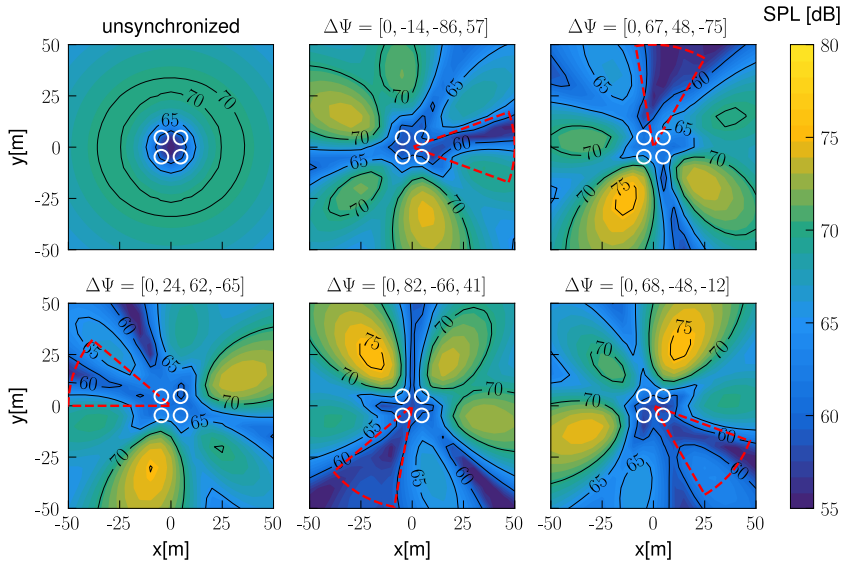

(a) Noise footprint of the quadrotor

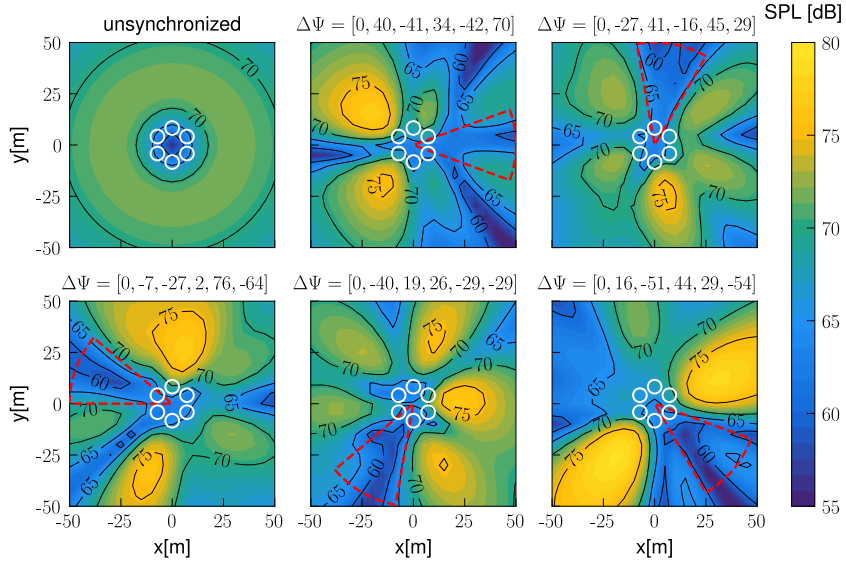

(b) Noise footprint of the hexarotor

Fig. 11. Contours of the SPL over the ground plane in hover for the reference case with unsynchronized rotors, and for test cases conducted with optimized rotor phases to obtain a minimum of SPL over the specified ground zone, which is highlighted with a dotted red line. Only five out of the nine considered optimization regions are shown. The white circles indicate the rotors positions and are not to scale. The ground plane is located 25 m below the vehicle. The shown contour lines correspond to levels of [60, 65, 70, 75] dB. (For interpretation of the references to colour in this figure legend, the reader is referred to the web version of this article.)

3. Selection: Parent solutions for the next generation are selected probabilistically, with fitter individuals having a higher chance of being chosen. A roulette wheel selection mechanism was used for this purpose.
4. Crossover and Mutation: Offspring are created by applying crossover (combining parent solutions) and mutation (introducing small, random perturbations) operators. These steps ensure a balance between exploiting promising regions of the search space and exploring new ones to avoid premature convergence to local minima.
5. Survival: The fittest individuals from the combined pool of parents and offspring are selected to form the population for the next iteration.

This process is repeated for a set of generations, or until the improvements in the best–found solution are not relevant anymore. The final output of the procedure is the optimized phase vector, $\Delta\Psi_{opt}$, which theoretically produces the maximum noise reduction in the targeted region. The effectiveness of these optimized phase angles is then verified using the complete UPM–APSIM simulation toolchain.

4.3. Results

In this subsection, we present some results of the toolchain for the hover flight condition using the setup described in Section 4.1. Since the aircraft is in hover, the phase vector was optimized with the previously introduced procedure based on the analytical tool (see Section 2.2). Two strategies were considered: Hemisphere and Ground optimization. The former is a quasi 1–D approach, consisting of a purely azimuthal optimization within a slice of the hemisphere that surrounds the configuration. The second approach instead considers a 2–D portion of the ground plane. As observed during the research, the ground optimization provided more reliable and effective results. For this

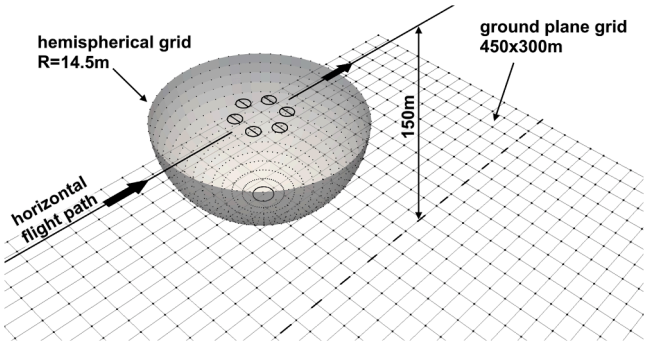

Fig. 12. Acoustic simulation domain for the flyover case. The multirotor is placed over a rectangular ground plane, on the longer symmetry line at a distance of 200 m from the left side, at a height of 150 m and inside a hemispherical microphone grid.

Table 7
Comparison of the average SPL [dB] calculated over the considered ground regions between the reference and the result of optimized phase shifting.

Region	Quadrotor	Hexarotor
−20° to 20°	60.4	63.4
20° to 60°	62.4	59.7
60° to 100°	57.9	61.7
100° to 140°	59.6	60.4
140° to 180°	61.3	61.5
180° to 220°	62.4	62.9
220° to 260°	58.1	60.7
260° to 300°	57.2	60.1
300° to 340°	59.4	60.9
Unsynchronized	68.5	70.3

reason, only this second approach is reported and discussed in the present work.

Fig. 11 shows the ground SPL footprint calculated with the UPM–APSIM toolchain for five of the nine total subregions for both the quadrotor and hexarotor cases. Each case corresponds to an optimized vector of phase angles, calculated in this case with the analytical model as explained in Section 4.2, written on top of each contour plot in the convention explained in Section 1.2. It can be noted that in the red–dotted areas, where minimization was requested, reduction regions are effectively present, explaining the results reported in Table 7. It can also be observed that some regions exhibit noise augmentation. These are of the same order of magnitude as the minimum ones (i.e., up to 10 dB). These regions are particularly important and must be taken into account when dealing with real world scenarios. In fact, in a hypothetical in–flight phase shift controller, it would be necessary to actively steer the acoustic field during flight to ensure that the target region consistently remains in a minimum rather than in a maximum.

Table 7 reports the optimization results for each slice spanning all the ground domain for the hexarotor and quadrotor configurations. Each row value is obtained by averaging the SPL in the region where noise reduction was requested by the user. For the computation of the unsynchronized reference case, see Section 2.1.3. The main outcome of this analysis is that noise directivity optimization is feasible for all domain subregions. In fact, despite the resulting outcomes varying slightly due to the optimizer efficiency, a consistent local average reduction of 8.6 dB for the quadrotor and 9.1 dB for the hexarotor was achieved, when compared to the unsynchronized domain.

5. Application to forward flight

Here we consider the quadrotor and hexarotor configurations under trimmed level forward flight conditions. As in the hover case, the aim was to adjust rotor phase angles to control the noise footprint and achieve local minima in the overall sound pressure level within targeted ground regions. Since the analytical model was not yet applicable to forward flight, the optimization had to employ the numerical toolchain. To reduce the computational time, a simplified simulation procedure was adopted which does not account for aerodynamic interactions between rotors and uses the output of a single aerodynamic simulation for an isolated rotor, in the test flight condition, to run the complete acoustic simulation. The results are then computed with the complete simulation procedure, using the optimized phase angles as an input.

Table 8
Parameters for the flyover test case.

Flight parameters	
Flight condition	Level forward flight
$\|\|\mathbf{TAS}\|\|$	28.33 m s^{-1}
Advance ratio μ	0.23
Tip Mach number M_t	0.43
Environment	150 m ISA +8 °C
UPM parameters	
Time step size	2°
Number of revolutions	12
Vortex core radius	$0.8 \cdot c_{75}$
Wake size	Restricted

5.1. Simulation setting

The distance between the horizontal flight path and the ground plane is set at 150 m, and the plane has dimensions of 450×300 m. The setup was designed in accordance with the EASA guidelines [27] as in the hover case. The trimmed flight condition and the simulation parameters are reported in Table 8. The wake in forward flight was restricted to a length of 2 rotor diameters behind the vehicle, under the hypothesis of it being of negligible influence at that distance. The computational domain is illustrated in Fig. 12. A hemispherical grid was also employed, same as in the hover case. The flight speed was chosen to be high enough such that the interaction of the aft rotors with the wake shed by the front ones did not strongly affect the acoustic emission. This depends mainly on the convection velocity of the wakes by the external flow and on the pitch down angle of the vehicle, which in this case is 9.3° for the quadrotor and 12.1° for the hexarotor.

Three zones were selected on ground in order to control the sound directivity: a front region located ahead of the vehicle, and two side regions. Each of them is a circular sector centered with the orthogonal projection of the vehicle, with a radius of 200 m and spanning through a range of 40°. Considering the azimuth angle being 0 on the x axis and positive counterclockwise from above, the front region goes from −20° to 20°, the port (left) region from 70° to 110° and the starboard (right) region from −70° to −110°.

5.2. Optimization procedure

The formulation of the optimization problem is as already explained in Section 4.2.1. Since in this case the optimization algorithm was applied to the numerical toolchain, a different approach was used based on surrogate modeling in order to reduce the number of required simulations. Additionaly, a simplified version of the toolchain was implemented neglecting aerodynamic interactions between rotors.

5.2.1. Fast aeroacoustic simulation with single rotor aerodynamic solution

The fundamental idea was that the interference between the aft rotors and the wakes shed by the front ones could be, in some flight conditions, weak enough to be neglected. This would happen for a sufficiently high flight speed and attitude pitch down angle, in order to avoid close interaction between the back rotors with the wake shed by the front ones. If this condition was not met, then the simulation

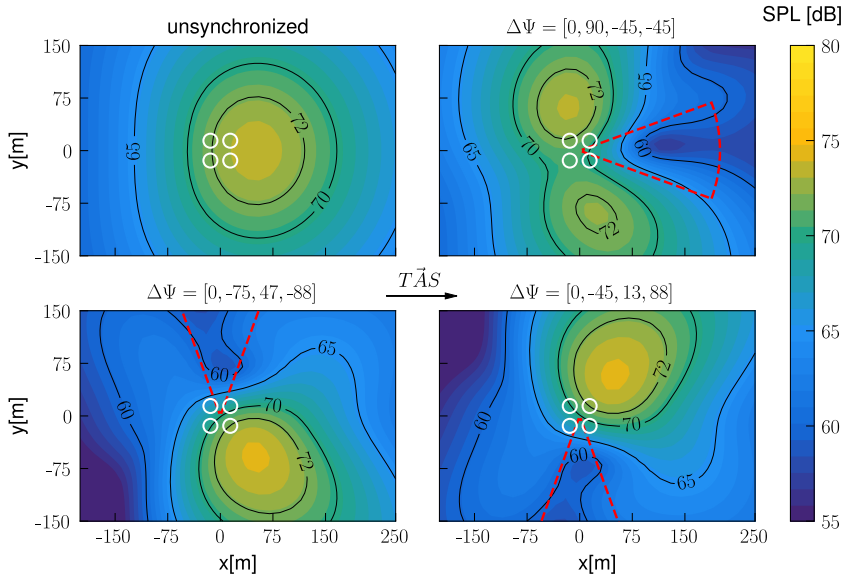

(a) Noise footprint of the quadrotor

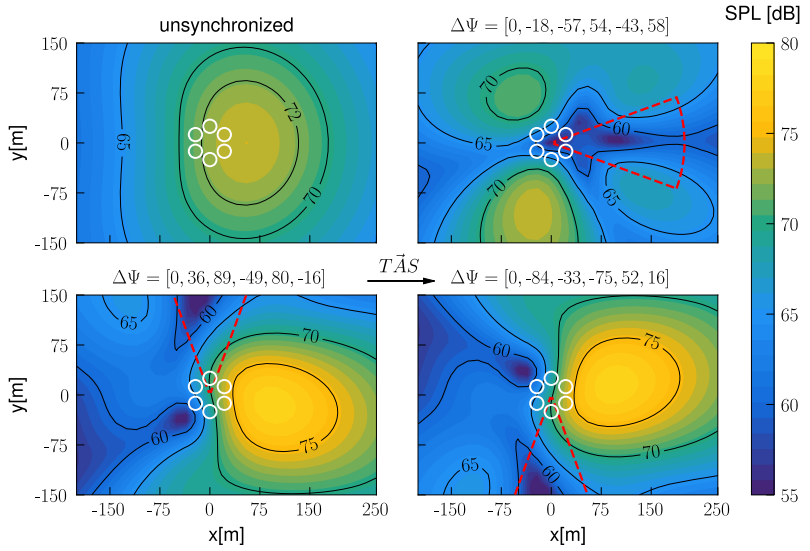

Fig. 13. Contours of the SPL over the ground plane in forward flight for the reference case with unsynchronized rotors, and for test cases conducted with optimized rotor phases to obtain a minimum of SPL over the specified ground zone, which is highlighted with a dotted red line. The white circles indicate the rotors positions and are not to scale. The vehicle flight direction goes from left to right, in the positive x axis direction. The advance ratio is 0.23. The ground plane is located 150 m below the vehicle. The shown contour lines correspond to levels of [60, 65, 70, 72, 75] dB. (For interpretation of the references to colour in this figure legend, the reader is referred to the web version of this article.)

results would be incorrect and the optimization would need to be applied to the complete aeroacoustic toolchain. Thus a custom toolchain was developed which performs a single aerodynamic simulation of an isolated rotor, in the same attitude and trim state as the complete configuration. The resulting grid files representing the rotor blades with the pressure distribution are then used to build the complete rotor configuration, by translating them into the correct position, and shifting them in time to adjust for phase angle. The resulting data can then be used to calculate the acoustic interference of phased rotors. This reduces drastically the required computation time not only because the UPM simulation considers only one rotor, but also because if the flight condition stays the same, it is possible to test different phase angles without having to recompute the aerodynamic solution and only perform the acoustic one. This procedure was used in the process of optimizing the phase angles which were then the input for the complete simulation.

5.2.2. *Surrogate based optimization*

The optimization software here adopted is the surrogate based optimization algorithm POT (Powerful Optimization Tools) with SuMo (Surrogate Modeling) developed by Gunther Wilke [29]. Surrogate based optimization (SBO) is a sub–group of numerical optimization strategies and is an acceleration mechanism for regular optimization. Through mathematical abstraction of the true function, here the simulation code, a quickly to evaluate surrogate is created. The search of the optimum in this surrogate is a lot faster than in the true function. However, this mathematical abstraction is likely to lack in accuracy compared to the true function and thus has to be improved in regions of interest.
Surrogate based optimization typically follows these steps:

1. Design of Experiments (DoE): Initial sampling of the design space using techniques such as Latin Hypercube Sampling or space–filling designs.

2. Surrogate Model Construction: Common models include Gaussian Processes, Radial Basis Functions, and Polynomial Regression.
3. Optimization and Refinement: While regular optimization directly searches for the best goal function, surrogate–based optimization requires adaptive sampling to find the best design. This means improving the surrogate model even in less relevant regions to confirm their insignificance. A proper optimization strategy and careful selection of algorithms are essential for choosing infill points. Depending on the order of the design space and on the application (global or local) different algorithms are employed, such as the Hooke and Jeeves pattern search, the Differential Evolutionary algorithm and the Simplex pattern search method.
4. Stopping Criteria: Optimization stops when a convergence criterion, such as function improvement or model confidence, is met.

5.3. Results

In Fig. 13 we see the ground noise contours for different optimization regions, together with the estimated unsynchronized case (see Section 2.1.3 for the computation of the reference acoustic emission), for both the quadrotor and the hexarotor. The noise carpets indicate how the optimization algorithm succeeded in finding the relative phase shift angles which would steer noise away from the specified region. Those are indicated on top of each contour plot and comply with the convention explained in Section 1.2. We can observe that the baseline noise carpet is similar for the two configurations, both with respect to the directivity (hexarotor footprint is a bit more expanded) and to the absolute SPL levels. The noise is concentrated slightly in front of the vehicle and is symmetrical about the flight direction, due to the symmetry in the rotors configuration.

The front optimization for the quadrotor produced two lobes of high noise level right at the sides of the vehicle, while reducing it for basically the whole right side of the plane, and not only for the specified region delimited in red. The side optimization instead moved the single concentration spot away from either the port or starboard side. We can note how the contours for those two cases look flipped around the x axis with respect to one another. In fact, the optimized phases are exactly mirrored between the two cases, producing in turn a mirrored noise carpet. This symmetry property was found to be related to the acoustic behavior of synchronized rotor pairs: a single couple of counter–rotating rotors with either tip–to–tip ($\Delta\Psi = 0°$) or orthogonal ($\Delta\Psi = 90°$) phasing emits sound waves symmetrically w.r.t. the plane between the rotors. Then any configuration involving couples of counter–rotating rotors all in either tip–to–tip or orthogonal phasing will show a symmetric noise emission, and this holds for forward flight if the flight direction lies on the plane of symmetry. A consequence is that for any phase distribution, inverting the values side to side w.r.t. the plane of symmetry causes the sound emission to be mirrored.

Table 9
Comparison of the average SPL [dB] calculated over the considered ground regions between the reference and the result of optimized phase shifting.

(a) Quadrotor

Region	Reference	Optimized
Front	71.1	61.5
Port	70.0	60.4
Starboard	70.0	60.4

(b) Hexarotor

Region	Reference	Optimized
Front	71.6	61.8
Port	70.6	62.9
Starboard	70.6	62.9

Looking at the hexarotor case, the optimization of the frontal region created four lobes of noise concentration on the ground, two stronger ones at the back and the other weaker two in the front, at the sides of the prescribed noise minimization zone. A stronger reduction is also obtained right under the vehicle with respect to the quadrotor case. The side optimization produces results similar to the quadrotor, steering noise away from the interest region where a local minimum appears, but in this case it also produces a strong constructive interference in the front increasing considerably the maximum SPL value. Table 9 shows the difference in the average value of SPL in the considered ground regions for the reference (no synchronization) case and the optimized one. A reduction of around 10 dB is achieved in all cases.

6. Conclusions

This work examines the performance of a noise reduction method based on rotor phase shifting through numerical simulations. A dedicated simulation toolchain predicts the acoustic emission of multirotors by employing the unsteady free–wake panel code UPM as the aerodynamic solver and coupling its output with the Ffowcs Williams–Hawkings acoustic solver APSIM to compute linear sound propagation at observer locations. The framework also includes the determination of trimmed flight conditions.

To achieve directional noise reduction through rotor phase control, optimization procedures are applied to quadrotor and hexarotor configurations in both hover and forward flight:

- Hover flight: A simplified analytical model based on compact sources is developed to estimate the noise directivity pattern and the effect of phase shifting. By applying a genetic optimization algorithm to this computationally efficient model, optimized phase vectors are obtained and subsequently evaluated using the high–fidelity simulation toolchain. The ground plane, located 25 m beneath the vehicle, is divided into nine circular sectors serving as optimization regions. Average sound pressure level (SPL) reductions of 8.6 dB for the quadrotor and 9.1 dB for the hexarotor are achieved across these zones.
- Forward flight: A surrogate–based optimization algorithm is applied directly to the full simulation framework. The ground plane, located 150 m below the vehicle flying at an advance ratio of $\mu = 0.23$, is partitioned into three optimization zones in front of and beside the multirotor. Average SPL reductions of 9.6 dB for the quadrotor and 8.4 dB for the hexarotor are achieved across these regions.

Overall, the main research objective has been achieved: the results showed that it is possible to control the noise directivity pattern of multirotor VTOL aircraft by implementing phase shifting in both hover and forward flight. This was done by considering the trim condition of the aircraft equipped with rotor pitch control, in order to allow for phase synchronization while maintaining constant rotor speed. Moreover, this new approach represents a step forward into real world implementation of such noise control, providing the baseline for quieter VTOL aircraft design without excessive hardware modifications. Furthermore, in hover, the simplified analytical model proves sufficient for determining optimal phase angles, highlighting its potential as a fast prediction tool and for future in–flight implementation. To this end, future developments aim to extend the model to forward flight and ultimately integrate it into a real–time onboard noise prediction system. Further research should investigate rotor–wake interaction effects across varying flight conditions and validate the findings for forward flight through experimental campaigns.

CRediT authorship contribution statement

Francesco Sessini: Writing – original draft, Visualization, Validation, Software, Methodology, Investigation, Data curation; **Diego**

Donnini: Writing – original draft, Visualization, Validation, Software, Methodology, Investigation, Data curation; **Aldo Chella:** Writing – original draft, Visualization, Validation, Software, Methodology, Investigation, Data curation; **Thorsten Schwarz:** Validation, Supervision, Software, Resources, Project administration, Methodology, Investigation, Funding acquisition, Data curation, Conceptualization; **Jianping Yin:** Validation, Supervision, Software, Resources, Project administration, Methodology, Investigation, Funding acquisition, Data curation, Conceptualization; **Gabriele Bellani:** Writing – review & editing, Validation, Supervision, Methodology, Formal analysis; **Emanuele L. de Angelis:** Writing – review & editing, Validation, Supervision, Methodology, Formal analysis.

Data availability

Data will be made available on request.

Declaration of competing interest

The authors declare that they have no known competing financial interests or personal relationships that could have appeared to influence the work reported in this paper.

Acknowledgment

This work was conducted as part of the Master's thesis of students A. Chella, D. Donnini, and F. Sessini of the University of Bologna, under the supervision of Profs. G. Bellani and E.L. de Angelis. The research was hosted by the Helicopter Department of the DLR Institute of Aerodynamics and Flow Technology, with the supervision of Drs. J. Olsman, T. Schwarz, and J. Yin.

References

[1] B.A. Hamilton, Urban Air Mobility (UAM) Market Study, Presented to NASA Aeronautics Research Mission Directorate, Technical Report HQ-E-DAA-TN65181, Report, 2018.
[2] A. Filippone, G.N. Barakos, Rotorcraft systems for urban air mobility: a reality check, Aeronaut. J. 125 (1283) 2021 3–21. https://doi.org/10.1017/aer.2020.52
[3] F.H. Schmitz, The challenges and possibilities of a truly quiet helicopter, Proc. Vertical Flight Soc. 61 (2016) 1–33. https://doi.org/10.4050/JAHS.61.041001
[4] ICAO Committeeon Aviation Environmental Protection Working Group, Helicopter Noise Reduction Technology: Status Report, Technical Report, Technical Report, 2015.
[5] B. Edwards, C. Cox, S.I.L.E.N.T. Program, Revolutionary Concepts for Helicopter Noise Reduction, Technical Report NASA ICR-2002-211650, NASA Aeronautics Research Mission Directorate, 2002.
[6] G. Wilke, Quieter and greener rotorcraft: concurrent aerodynamic and acoustic optimization, CEAS Aeronaut. J. 12 (2021) 495–508. https://doi.org/10.1007/s13272-021-00513-x
[7] N.H. Schiller, K.A. Pascioni, N.S. Zawodny, Tonal noise control using rotor phase synchronization, in: Proc. of the 75t Annual Forum and Technology Display of the Vertical Flight Society, 75th Annual Forum and Technology Display of the Vertical Flight SocietyPhiladelphia, USA, 2019, pp. 1–12. https://doi.org/10.4050/F-0075-2019-14455
[8] K.A. Pascioni, S.A. Rizzi, N.H. Schiller, Noise reduction potential of phase control for distributed propulsion vehicles, in: Proc. of the AIAA Science and Technology Forum, AIAA Science and Technology ForumSan Diego, USA, 2019, pp. 1–10. https://doi.org/10.2514/6.2019-1069
[9] S. Guan, Y. Lu, T. Su, X. Xu, Noise attenuation of quadrotor using phase synchronization method, Aerosp. Sci. Technol. 118 (9) (2021) 107018. https://doi.org/10.1016/j.ast.2021.107018
[10] B. Smith, F. Gandhi, A. Lyrintzis, An assessment of multicopter noise in edgewise flight, in: Proc. of the 77th Annual Forum and Technology Display of the Vertical Flight Society, Virtual Event, of the 77th Annual Forum and Technology Display of the Vertical Flight Society, Virtual Event, 2021, pp. 1–13. https://doi.org/10.4050/F-0077-2021-16691
[11] B. Smith, F. Gandhi, R. Niemiec, A comparison of tonal noise characteristics of large multicopters with phased rotors, J. Am Helicopter Soc. 68 (3) (2023) 032008. https://doi.org/10.4050/JAHS.68.032008
[12] B. Smith, F. Gandhi, Quadcopter noise variation due to relative rotor phasing, in: Proc. of the 80th Annual Forum and Technology Display of the Vertical Flight Society, of the 80th Annual Forum and Technology Display of the Vertical Flight Society, 2024, pp. 1–10. https://doi.org/10.4050/F-0080-2024-1335
[13] A. Patterson, K. Ackerman, A. Gahlawat, N. Hovakimyan, N.H. Schiller, I. Gregory, Controller design for propeller phase synchronization with aeroacoustic performance metrics, in: Proc. of the AIAA Science and Technology Forum, of the AIAA Science and Technology ForumOrlando, USA, 2020, pp. 1–12. https://doi.org/10.2514/6.2020-1494
[14] T.V. Valente, E.N. Johnson, E. Greenwood, Implementation of a phase synchronization algorithm for multirotor UAVs, in: Proc. of the IEEE/AIAA 41st Digital Avionics Systems Conference (DASC), 2022, pp. 1–6. https://doi.org/10.1109/DASC55683.2022.9925771
[15] T.V. Valente, E. Greenwood, E.N. Johnson, An experimental evaluation of an electronic rotor phase synchronization system for multirotor aircraft noise control, in: Proc. of the 80th Annual Forum and Technology Display of the Vertical Flight Society, 2024, pp. 1–15. https://doi.org/10.4050/F-0080-2024-1194
[16] M. Mckay, R. Niemiec, F. Gandhi, Performance comparison of quadcopters with variable-RPM and variable-pitch rotors, J. Am. Helicopter Soc. 64 (4) (2019) 1–14. https://doi.org/10.4050/JAHS.64.042006
[17] C. Malpica, S. Withrow-Maser, Handling qualities analysis of blade pitch and rotor speed controlled eVTOL quadrotor concepts for urban air mobility, in: Proc. of the VFS International Powered Lift Conference, VFS International Powered Lift ConferenceSan Jose, USA, 2020, p. 214590210. https://api.semanticscholar.org/CorpusID.
[18] R. Porter, B. Shirinzadeh, M.H. Choi, Experimental analysis of variable collective-pitch rotor systems for multirotor helicopter applications, J. Intell. Robot. Syst. 83 (2) (2016) 271–288. https://doi.org/10.1007/s10846-015-0311-2
[19] S. Sheng, C. Sun, Control and optimization of a variable-pitch quadrotor with minimum power consumption, Energies 9 (4) (2016) 232. https://doi.org/10.3390/en9040232
[20] M. Cutler, N.-K. Ure, B. Michini, J.P. How, Comparison of fixed and variable pitch actuators for agile quadrotors, in: Proc. of the AIAA Guidance, Navigation, and Control Conference, AIAA Guidance, Navigation, and Control ConferenceSan Diego, USA, 2011, pp. 1–10. https://doi.org/10.2514/6.2011-6406
[21] P. Kunze, A panel free-wake code with boundary layer method for helicopter simulations, in: Proc. of the 45th European Rotorcraft Forum, 45th European Rotorcraft ForumWarsaw, Poland, 2019, pp. 1–10.
[22] J. Yin, K.-S. Rossignol, L. Rottmann, T. Schwarz, Numerical studies on small rotor configurations with validation using acoustic wind tunnel data, CEAS Aeronaut. J. 15 (2023) 671–702. https://doi.org/10.1007/s13272-023-00671-0
[23] S. Miesner, M. Keßler, E. Krämer, U. Schäferlein, High-fidelity simulation of the Volocopter-2X in cruise flight, in: Proc. of the 77th Annual Forum of the Vertical Flight Society, 2021, pp. 1–13. https://doi.org/10.4050/F-0077-2021-16724
[24] J. Delfs, Technical Report, TU Braunschweig, Institut für Aerodynamik und Strömungstechnik, 2022. Grundlagen der Aeroakustik (Basics of Aeroacoustics).
[25] L.V. Lopes, Compact assumption applied to monopole term of Farassat's formulations, J. Aircr. 54 (5) (2017) 1649–1663. https://doi.org/10.2514/1.C034048
[26] S.W. Rienstra, A. Hirschberg, An Introduction to Acoustics, Technical Report, Eindhoven University of Technology, 2017.
[27] Environmental Protection Technical Specifications Applicable to VTOL-Capable Aircraft Powered by Non-Tilting Rotors, Technical Report EU) 2018/139, EASA Technical Report, 2023. III.
[28] D.E. Goldberg, Genetic Algorithms in Search, Optimization, and Machine Learning, Addison-Wesley, New York, New York, 1989.
[29] G. Wilke, Variable-fidelity methodology for the aerodynamic optimization of helicopter rotors, AIAA J. 57 (8) (2019) 3145–3158. https://doi.org/10.2514/1.J056486